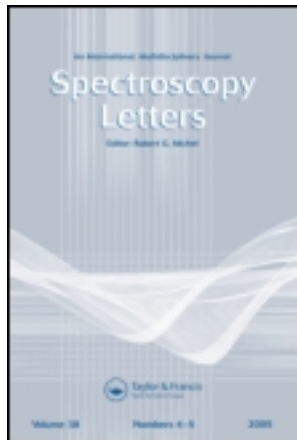


This article was downloaded by: [Xi'an University of Technology], [Shichun Li]

On: 31 December 2013, At: 22:54

Publisher: Taylor & Francis

Informa Ltd Registered in England and Wales Registered Number: 1072954 Registered office: Mortimer House, 37-41 Mortimer Street, London W1T 3JH, UK



Spectroscopy Letters: An International Journal for Rapid Communication

Publication details, including instructions for authors and subscription information:

<http://www.tandfonline.com/loi/Istl20>

All-Fiber Spectroscope with Second-Order Fiber Bragg Grating for Rotational Raman Lidar

Shichun Li^a, Dengxin Hua^a, Liaolin Hu^a, Qing Yan^a & Xiaoyu Tian^a

^a School of Mechanical and Precision Instrument Engineering, Xi'an University of Technology, Xi'an, China

Accepted author version posted online: 16 May 2013. Published online: 27 Dec 2014.

To cite this article: Shichun Li, Dengxin Hua, Liaolin Hu, Qing Yan & Xiaoyu Tian (2014) All-Fiber Spectroscope with Second-Order Fiber Bragg Grating for Rotational Raman Lidar, Spectroscopy Letters: An International Journal for Rapid Communication, 47:3, 244-252, DOI: [10.1080/00387010.2013.795173](https://doi.org/10.1080/00387010.2013.795173)

To link to this article: <http://dx.doi.org/10.1080/00387010.2013.795173>

PLEASE SCROLL DOWN FOR ARTICLE

Taylor & Francis makes every effort to ensure the accuracy of all the information (the "Content") contained in the publications on our platform. However, Taylor & Francis, our agents, and our licensors make no representations or warranties whatsoever as to the accuracy, completeness, or suitability for any purpose of the Content. Any opinions and views expressed in this publication are the opinions and views of the authors, and are not the views of or endorsed by Taylor & Francis. The accuracy of the Content should not be relied upon and should be independently verified with primary sources of information. Taylor and Francis shall not be liable for any losses, actions, claims, proceedings, demands, costs, expenses, damages, and other liabilities whatsoever or howsoever caused arising directly or indirectly in connection with, in relation to or arising out of the use of the Content.

This article may be used for research, teaching, and private study purposes. Any substantial or systematic reproduction, redistribution, reselling, loan, sub-licensing, systematic supply, or distribution in any form to anyone is expressly forbidden. Terms & Conditions of access and use can be found at <http://www.tandfonline.com/page/terms-and-conditions>

All-Fiber Spectroscope with Second-Order Fiber Bragg Grating for Rotational Raman Lidar

Shichun Li,
Dengxin Hua,
Liaolin Hu,
Qing Yan,
and Xiaoyu Tian

School of Mechanical and
Precision Instrument
Engineering, Xi'an University of
Technology, Xi'an, China

ABSTRACT Owing to the second-order fiber Bragg grating possessing narrower reflectivity bandwidth than first-order, an all-fiber spectroscopic filter with several second-order fiber Bragg gratings and optical fiber couplers in the visible region is designed to extract interest rotational Raman spectra. Considering the inference fringe visibility of inscribing fiber Bragg grating and the fiber core index dispersion effect, numerical simulations are made by the improved mathematical model based on an exponential photorefractive dynamic, and its simulative results show better agreement with the experimental data. We propose an all-fiber spectroscopic configuration, which could balance lidar sensitivity against signal-to-noise ratio for optimizing remote sensing performance by fiber Bragg gratings serially. Simulative results show that the thumb principle for fabricating second-order fiber Bragg grating is the increasing gratings length, and that this all-fiber spectroscope can achieve >70 dB suppression to elastic scattering and efficiently extract the rotational Raman signal for profiling atmospheric temperature.

KEYWORDS all-fiber spectroscope, exponential photorefractive dynamic, rotational Raman lidar, second-order fiber Bragg grating

INTRODUCTION

The rotational Raman lidar (RRL) has been widely applied to the atmosphere science field for remote sensing atmospheric temperature due to its higher temporal and spatial resolution.^[1] Several spectroscopic techniques for RRL have been demonstrated in recent years, including double-grating monochromator or polychromator,^[2] double interference filters,^[3] and grating spectrometer together with an atomic vapor filter.^[4] These spectroscopes in general adopt two cascades of spectroscopic devices to provide approximately 70–80 dB suppression of elastic backscattering. Arshinov et al. applied a Fabry-Perot interferometer as a frequency comb filter to remove the sky background between the rotational Raman spectral lines of nitrogen molecules.^[5] In order to decrease the adjustment complexity and the volume or weight of the lidar spectroscope for propelling the satellite-borne or vehicle-borne lidar system, Vann et al. applied first-order fiber Bragg grating

Received 28 January 2013;
accepted 9 April 2013.

Address correspondence to
Dengxin Hua, School of Mechanical
and Precision Instrument
Engineering, Xi'an University of
Technology, No. 5 South Jinhua Road,
Xi'an 710048, China. E-mail:
dengxinhua@xaut.edu.cn

(FBG) to differential absorption lidar for atmospheric water vapor and fabricated a narrowband fiber-optic phase-shifted Fabry-Perot Bragg grating filter at a wavelength of 946 nm.^[6] Liu et al. put forward utilizing the first-order FBG at a wavelength of 589 nm for Na fluorescence lidar.^[7] Mao et al. of our research group also proposed a pure rotational Raman lidar with a first-order FBG spectroscopy for profiling the atmospheric temperature.^[8] Because the reflectivity bandwidth of a second-order FBG is generally narrower than that of first-order, it is reasonable to adopt the second-order FBG for blocking the sky background between the rotational Raman spectral lines. Moreover, since the reflectivity bandwidth is directly relevant to the period accuracy or uniformity of the zero-order nulled phase mask,^[9] the high period accuracy of the phase mask is required to remove the sky background. Therefore, second-order FBG is proposed to obtain narrow reflectivity bandwidth and degrade this requirement of phase mask.

FBG has been applied in communication and fiber sensor fields due to its excellent spectroscopic property and inherent compatibility with optical fiber.^[10–12] Since Xie et al. reported the second-order FBG,^[13] the higher-order FBG technique has been studied owing to its particular properties such as multiparameter discrimination in the sensing field,^[14,15] the abilities of a high-order operator,^[16] and strong polarization with a suitable tilt angle.^[17] So far the second-order FBG has mainly been applied in strain-temperature sensors^[15] and fiber laser fields.^[17] Our interest to this subject is connected with the possibility of exploitation of an all-fiber Raman spectroscopy with second-order FBG to extract interest rotational Raman spectra.

Comparing with current mathematical models of fiber gratings growth based on the photorefractive saturation effects,^[18–21] the mathematical model based on the coupled-mode theory and the exponential photorefractive dynamic is enhanced and discussed according to the all formula in the Theoretical Analysis section. The relationship between first-order and second-order resonance wavelength is modeled by considering the fiber core index dispersion effect and the core power confinement factor of the guide mode, and discussed for selecting suitable phase masks. In the System Configuration section, an all-fiber second-order FBG spectroscopic configuration is put forward, which is provided with good

flexibility and to achieve a balance of lidar sensitivity against the signal-to-noise ratio by FBGs in serial. We analyze in detail the influence of FBG fabricating parameters on performance of second-order FBG and show the core principle of fabricating second-order FBG for this all-fiber spectroscopic filter in the FBG Performance Discussion section.

THEORETICAL ANALYSIS

FBG is a periodic perturbation of the refractive index in fiber core, fabricated by exposing a photosensitive fiber to a spatially varying pattern of ultraviolet intensity.^[22] The refractive index change Δn is generally linearly related to the number of absorption photons through the Kramers-Kronig relation, and is given as:^[19]

$$\Delta n = \Delta n_s \cdot \left[1 - \exp\left(-\frac{P \cdot t}{E_s}\right) \right] \quad (1)$$

where P is incident optical power, t is the exposure time, and Δn_s and E_s represent the saturation index variation and the saturation energy, respectively, which mainly depend on the core dopant concentration of the photorefractive fiber and are generally determined by experiments.

If the transverse index variation in the fiber core is negligible, the mathematical model of the spatial index variation $\Delta n(x, y, z)$ can be simplified and only the refractive index perturbation along the fiber length considered, that is, $\Delta n(z)$.^[13,19] Considering the interference fringe visibility v_f of inscribing FBG,^[22] the refractive index of fiber core can be represented by:

$$n(z) = n_{co} + \Delta n(z) = n_{co} + \Delta n_s \cdot n_{nr}(z) \quad (2)$$

where n_{co} is the core refractive index without perturbation for the fiber, and $n_{nr}(z)$ represents the normalized core refractive index change shown in Fig. 1 for different exposure times, and may be described as:

$$n_{nr}(z) = \frac{\Delta n(z)}{\Delta n_s} = 1 - \exp\left\{-\frac{P_0 \cdot A(z)}{2E_s} [1 + v_f \cdot \cos(\varphi(z))] \cdot t\right\} \quad (3)$$

where P_0 is the peak optical power of the interference pattern, $A(z)$ is the normalized apodization function and is unity for uniform FBG, and $\varphi(z)$ is the phase

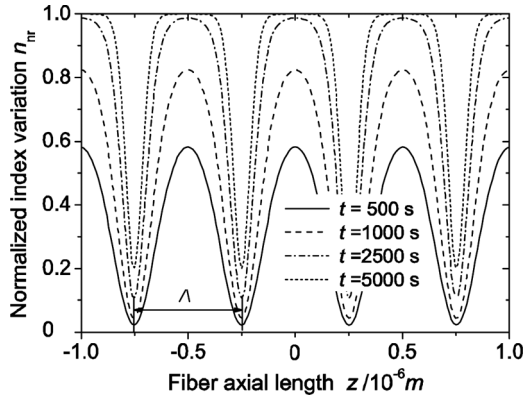


FIGURE 1 Formation process of normalized photorefractive perturbation along fiber length.

in radian, which is related to the interference period $\Lambda(z)$ by:^[19]

$$\varphi(z) = \int_0^z \frac{\pi}{\Lambda(z')} dz' \quad (4)$$

and is $\pi \cdot z/\Lambda$ for unchirped FBG.

The forming process of the normalized photorefractive perturbation with several exposure time instants is demonstrated in Fig. 1; the parameters are as follows: $E_s = 140$ J, $P_0 = 250$ mW, and $v_f = 0.95$. It is clear that the normalized index variation is not zero in valley and increases with the exposure time. As the exposure time passes, the maximum refractive index change is gradually close to the saturation index change, and the index change along the fiber length deviates gradually from the standard sinusoidal distribution. Therefore, the high order (>1) Bragg resonances appear, which agrees with the experimentally observed phenomenon.^[18,19] The influence and magnitude of the new resonance periodic components may be shown by expanding the normalized refractive index perturbation as a Fourier series as follows:^[18,23]

$$n_{nr}(z) = G_0 + \sum_{m=1}^{\infty} G_m \cos\left(m \frac{2\pi}{\Lambda} z\right) \quad (5)$$

where Λ is the grating period, G_0 is the average refractive index change, and the coefficient of the individual Fourier series term G_m is given as:

$$G_m = \begin{cases} \frac{1}{\Lambda} \int_{-0.5\Lambda}^{0.5\Lambda} n_{nr}(z) dz & m = 0 \\ \frac{2}{\Lambda} \int_{-0.5\Lambda}^{0.5\Lambda} n_{nr}(z) \cos\left(m \frac{2\pi}{\Lambda} z\right) dz & m > 0 \end{cases} \quad (6)$$

Figure 2 shows the influence of the exposure time on different order resonances. It is clear that the average refractive index change G_0 increases with the exposure time, and hence the central wavelength of FBG increases with the exposure time passing owing to its proportional relation with G_0 .^[18,19] Furthermore, the tendency of the FBG central wavelength is strengthened as the fringe visibility deviates from unity. It is also shown from Fig. 2 that the first-order and second-order coefficients are decreased as the fringe visibility deviates from unity. According to the Bragg condition,^[19] each of these components ($m > 0$) originates one Bragg resonance in the FBG spectral characteristic. These coefficients G_m ($m > 0$) may affect the peak reflectivity and bandwidth of m th order resonance.^[19]

Coupled-mode theory is a good tool for analyzing quantitative information about the reflectivity and spectral characteristics of FBG. The coupled-wave equation can be written as:^[22]

$$\begin{cases} \frac{dT(z)}{dz} = i \cdot \sigma \cdot T(z) + i \cdot \kappa \cdot R(z) \\ \frac{dR(z)}{dz} = -i \cdot \sigma \cdot R(z) - i \cdot \kappa^* \cdot T(z) \end{cases} \quad (7)$$

where $T(z)$ and $R(z)$ are the forward and backward waves in the fiber, that is, $T(z) = A(z)\exp(i \cdot \sigma \cdot z - 0.5\varphi)$, $R(z) = B(z)\exp(-i \cdot \sigma \cdot z + 0.5\varphi)$; $A(z)$ and $B(z)$ are the slowly varying amplitudes of the forward and backward waves, respectively, and κ is the ‘‘AC’’ coupling coefficient^[22] and may be represented for a single-mode Bragg gratings as:

$$\kappa = \kappa^* = \frac{\pi}{m \cdot \lambda} \cdot \delta n_{eff}^m \quad (8)$$

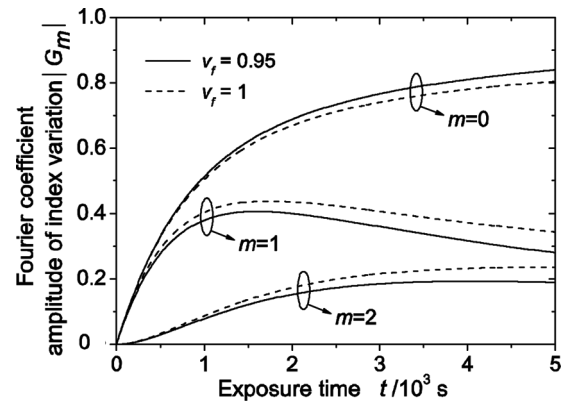


FIGURE 2 Fourier-series coefficients as a function of exposure time.

where δn_{eff}^m is the m th order modulation depth of effective index n_{eff} and may be described as:^[18,21]

$$\delta n_{\text{eff}}^m = \Gamma \cdot \delta n_{\text{co}}^m = \Gamma \cdot \Delta n_s \cdot G_m \quad (9)$$

where Γ is the core power confinement factor for the guide mode,^[22] and δn_{co}^m is the m th order diffraction modulation depth of the fiber core index. The detune factor σ may be described as

$$\sigma = \beta - \frac{m \cdot \pi}{\Lambda} = 2\pi \cdot n_{\text{eff}} \cdot (\lambda^{-1} - \lambda_B^{-1}) \quad (10)$$

where β is the propagating constant of fiber guide mode, and λ_B is the m th order Bragg resonance wavelength, which is given by

$$\lambda_B = \frac{2}{m} \cdot n_{\text{eff}} \cdot \Lambda \quad (11)$$

where n_{eff} is the effective index of the guide mode in perturbation fiber, and may be represented as:

$$n_{\text{eff}} = n_{\text{ef}} + \Gamma \cdot \Delta n_s \cdot G_0 \quad (12)$$

where n_{ef} is the effective index of the guide mode in unperturbed fiber, and is given as:

$$b = \frac{n_{\text{ef}}^2 - n_{\text{cl}}^2}{n_{\text{co}}^2 - n_{\text{cl}}^2} \quad (13)$$

where b is the normalized effective index parameter, and n_{cl} is the cladding index of the fiber.

Since the effective index n_{ef} and the core power confinement factor Γ of the guide mode are generally dependent upon the operation wavelength, Eq. (12) may be rewritten as:

$$n_{\text{eff}}(\lambda) = n_{\text{ef}}(\lambda) + \Gamma(\lambda) \cdot \Delta n_s \cdot G_0 \quad (14)$$

Therefore, the ratio of the first-order Bragg resonance wavelength to the second-order^[13] is not exactly 2, and then Eq. (11) may be rewritten as:

$$\lambda_B = \frac{2}{m} \cdot n_{\text{eff}}(\lambda_B) \cdot \Lambda \quad (15)$$

The dispersion function of refractive index $n(\lambda)$ for the fused silica may be described by Sellmeier formulas:

$$n^2(\lambda) - 1 = \frac{K_1 \lambda^2}{\lambda^2 - L_1} + \frac{K_2 \lambda^2}{\lambda^2 - L_2} + \frac{K_3 \lambda^2}{\lambda^2 - L_3} \quad (16)$$

where L_1 , L_2 , and L_3 are related to the square of three resonance wavelengths of material, and K_1 , K_2 , and

K_3 are the resonant intensity coefficients corresponding to individual resonance wavelength.

Considering the boundary condition of $T(-L/2) = 1$ and $R(L/2) = 0$ for gratings length L , the reflectivity R of FBG may be represented by:^[22]

$$R = \frac{\kappa^2 \sinh^2(\sqrt{\kappa^2 - \sigma^2} L)}{\sigma^2 \sinh^2(\sqrt{\kappa^2 - \sigma^2} L) + (\kappa^2 - \sigma^2) \cosh^2(\sqrt{\kappa^2 - \sigma^2} L)} \quad (17)$$

and the maximum reflectivity can be obtained at $\lambda = \lambda_B$, and may be described as

$$R_{\text{max}} = \tanh^2(\kappa \cdot L) \quad (18)$$

The numerically simulative results are compared with the experimental records of reference [13], as shown in Fig. 3. $\Delta n_s = 8 \times 10^{-4}$, $L = 6$ mm, and other parameters are identical to Fig. 2. Assuming we are not considering fringe visibility, that is, $v_f = 1$, the deviations become considerably larger between the simulation results and the experimental data. However, good agreement can be achieved at the fringe visibility of 0.95. While the exposure time is approximately 4000 s corresponding to 40,000 laser pulses (the laser pulse frequency is 10 Hz and the pulse duration is 20 ns^[13]), the maximum reflectivity is achieved. The obvious second-order resonance phenomenon appears at the exposure time of 500 s, corresponding to the reflectivity of the first-order resonance turning to a gradual increase. The first-order resonance tends to saturation at 1000 s, corresponding to the second-order resonance

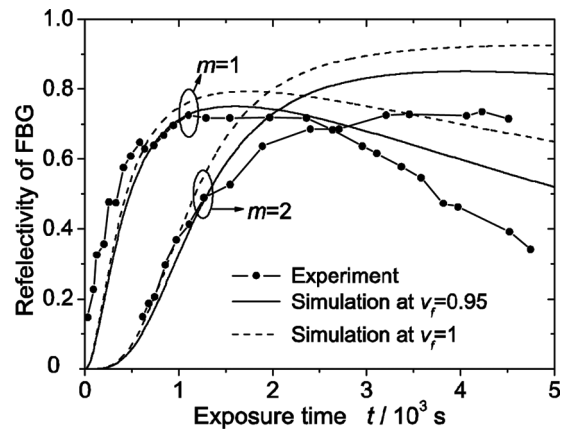


FIGURE 3 First- and second-order Bragg maximum reflectivity as exposure time varies.

quickly increasing. Furthermore, considering the dispersion influence on the Bragg resonant wavelength, the numerically simulated Bragg wavelength for first-order resonance at exposure time of 4000 s is 1451.8 nm, and its value for second-order is 732.5 nm, very close to the experimental value with 1451 nm and 734 nm.

SYSTEM CONFIGURATION

The dependence of low- and high-quantum-number rotational Raman backscattering intensity of atmospheric diatomic molecules such as nitrogen (N_2) and oxygen (O_2) on temperature is the theoretical basis of RRL operating. The atmospheric molecule backscattering cross-sectional area is in common inversely proportional to the fourth power of the excited laser wavelength. However, the operating central wavelength of FBG is shorter, and its fabricating technique is more difficult. Therefore, a narrowband, double-frequency, pulsed Nd:YAG laser with 532-nm wavelength is chosen as the exciting optical source. The laser beam is collimated by beam expander and transmitted into the atmosphere. The backscattering light is received by a Cassegrain telescope Mewlon-250 (TAKAHASHI, Japan) in our laboratory (Xi'an, China) with clear aperture 250 mm.

Since the rotational Raman scattering cross-section is less than three to four orders of magnitude compared to Mie and Rayleigh elastic scattering, the spectroscopic filter of RRL must at least provide 70–80 dB suppression of elastic scattering to efficiently retrieve the atmospheric temperature.^[8] However, the current optical filter in general only has out-of-band rejection of 30–40 dB including interfere filter, diffractive grating, and FBG, so the Raman channel of RRL needs twice the filtering. Figure 4 shows a configuration of an all-fiber RRL spectroscopic filter. Considering the higher fabrication cost of the optical circulator at 532-nm wavelength, we utilize a fiber coupler (FC) to substitute for the optical circulator, although theoretically it will introduce energy attenuation of 3 dB.

Since the first-order FBG may provide a reflectivity of more than 99.9%, this type of FBG with central wavelength (CW) 532 nm can be used as a one-stage filter to reflect the elastic scattering signal.^[8] However the second-order FBG generally provided a reflectivity of less than 90%; thus, we here adopt twice

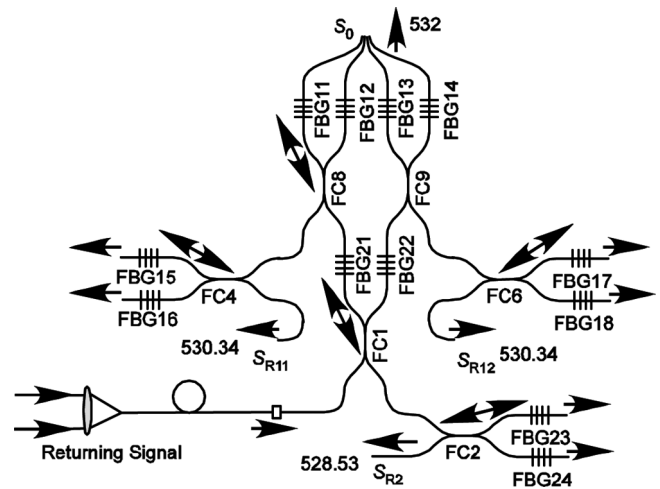


FIGURE 4 All-fiber RRL spectroscopic filter using second-order FBG. FBG11–FBG18 CW 530.34 nm, FBG21–FBG24 CW 528.53 nm.

reflection for providing 70–80 dB suppression of elastic scattering. If the reflection of FBG is about 80% (0.97 dB loss), the rotational Raman signal reflects two times by FBGs and is subject to 2 dB loss. Since FC usually possesses an excess loss of 0.8 dB and the signal passes four times through FCs, the loss in total is about 5 dB. Because the high-quantum-number Raman signal is weaker than the low-quantum-number Raman signal, we first extract the high-quantum-number Raman signal from the returning optical signal by FBG21 and FBG22 with CW 528.53 nm. The reflecting optical signal is then reflected through FBG23 and FBG24, and the high-quantum-number Raman signal S_{R2} is transmitted from one terminate port of FC2. Due to using FC1, the optical signal is split into two parts. The part of the low-quantum-number Raman signal S_{R11} is filtered by reflecting by FBG11 and FBG12 and then reflecting by FBG15 and FBG16. The other part S_{R12} is extracted by reflecting by FBG13 and FBG14 and then reflecting by FBG17 and FBG18. For achieving 70–80 dB suppression of elastic scattering, these FBGs require the reflectivity ratio of on-band to out-of-band of approximately 35–40 dB, which may be obtained in the current technique level.

Due to applying identical performance FBG, this layout should have a lower cost. Figure 5 shows a spectral characteristic of FBG1x (x is from 1 to 8) corresponding to $J=6$ and FBG2x (x is from 1 to 4) to $J=14$, where J is the rotational quantum number, together with the intensity of anti-Stokes rotational

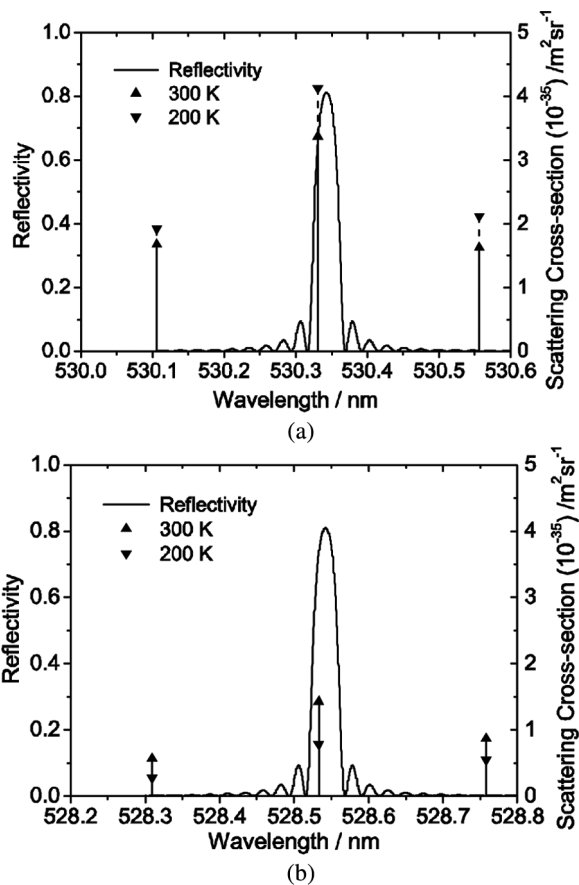


FIGURE 5 FBG spectroscopic characteristic and the anti-Stokes rotational Raman spectral intensity of nitrogen molecules: (a) low-quantum-number $J = 7, 6, 5$ (left to right); (b) high-quantum-number $J = 13, 12, 11$ (left to right).

Raman spectral lines of nitrogen molecules with adjacent quantum number at different temperature. The single spectral line may be filtered with narrow pass-band. Here, the gratings period is 362.12 nm and 360.87 nm, respectively, and the other parameters are as follows for 460-HP single-mode fiber: $\Delta n_s = 8 \times 10^{-4}$, $L = 4$ mm, $t = 3500$ s. The FBG shown in Fig. 5(a) has the second-order CW 530.34 nm corresponding to first-order 1050.2 nm. The FBG shown in Fig. 5(b) has the second-order CW 528.54 nm corresponding to first-order 1047.0 nm.

In order to avoid the influence of atmospheric fluorescence generated from laser excitation and enhance the temperature detection sensitivity of RRL, the anti-Stokes branch is chosen. For example, the spectroscopic filter shown in Fig. 4 only adopts the high-quantum-number ($J=14$) and the low-quantum-number ($J=6$) Raman spectral lines in the anti-Stokes branch. In some cases, however, the corresponding spectral lines in the anti-Stokes and

Stokes branches are simultaneously filtered to improve the Raman signal energy.^[24] Furthermore, in many cases the wider pass-band of the spectroscopic filter channel is selected to enhance the signal-to-noise ratio (SNR) of the Raman channel and then reduce the statistic error of atmospheric temperature, although this could result in lower sensitivity.^[8,26] Therefore, the optimum is necessary for lidar to balance the bandwidth of the Raman channel and system sensitivity. The spectroscopic filter designed in this article may easily achieve this optimum. By adding a set of FBGs to the FBGs of this spectroscopic filter in serial, whose CW is equal to the other quantum-number Raman spectral lines, the bandwidth of filtered Raman signal may be increased, and then the Raman signal intensity would be enhanced. For example, we can extract the high-quantum-number Raman signal to obtain better SNR by adding a set of FBGs with CW 528.08 nm ($J=14$) to FBG21–FBG24 in serial. Therefore, this spectroscopic filter has excellent flexibility or openness.

FBG PERFORMANCE DISCUSSION

The spectral characteristics of second-order FBG may in general be described by CW, maximum reflectivity, full width at half maximum (FWHM), and out-of-band rejection. Here, owing to the requirement of 70–80 dB suppression of elastic scattering, the out-of-band rejection of second-order FBG has become the most important parameter. There are a lot of fabricating parameters such as saturation index variation, grating length, exposure time, fringe visibility, and grating period required to be adjusted before photo-imprinting FBG. The grating period mainly affects the resonant CW. The fringe visibility depends generally on the optical arrangement and the period accuracy of the phase mask, and it is closer to unity, the FBG obtained has better performance (refer to Fig. 3). Since these FBGs in this spectroscopic filter have similar performance except for CW (e.g., their FWHMs are approximately 0.04 nm), this may cut down the fabrication cost of FBG. Moreover, their FWHM is narrower than that of first-order by comparison with the FWHM of these two types of FBGs in Fig. 6, and this has also been verified.^[19,25] Therefore, these second-order FBGs may cut out more sky background between the rotational Raman spectral lines.

We place emphasis on discussing the performance influences of low-quantum-number ($J=6$) FBG due

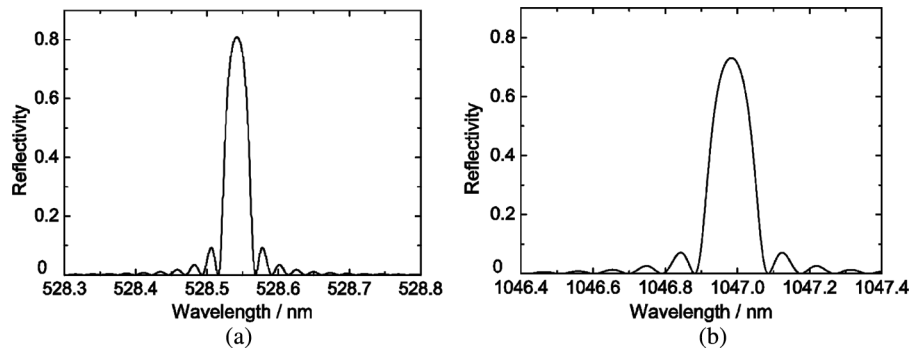


FIGURE 6 FWHM comparison of (a) the second-order FBG and (b) the first-order FBG.

to its being closer to the excited laser wavelength. Figure 7 shows the influences of three parameters on the out-of-band rejection and maximum reflectivity. It is particularly noted that the horizontal ordinates of Figure 7(a–c) all correspond to the curve of the solid line and that the horizontal ordinates of the dashed line and dotted dashed line are respectively shifted by 0.1 nm to the left and right for demonstrating more clarity. Figure 7(a) shows that the saturation index variation Δn_s has larger effects on out-of-band rejection of FBG and maximum

reflectivity. Although the greater saturation index variations can increase maximum reflectivity, they also could decrease out-of-band rejection. Figure 7(b) demonstrates that the longer grating length L has a advantage for the higher maximum reflectivity of FBG, and that this measure or means has little influence on the out-of-band rejection. Therefore, it is feasible for this spectroscope to improve the performance of FBG by extending the grating length. Although this measure generally increases the group dispersion of the optical signal

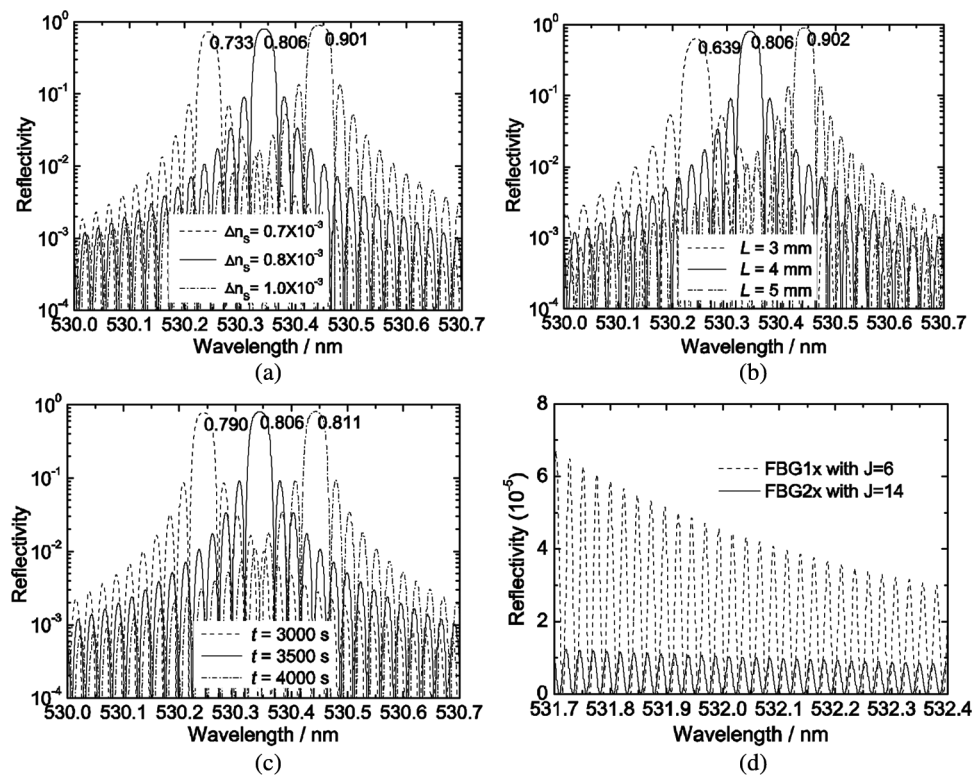


FIGURE 7 Performance variants of FBG as fabricating parameters: (a) the saturation index variation; (b) the longer grating length; (c) the exposure time; and (d) the out-of-band rejection of different FBGs, while $\Delta n_s = 0.8 \times 10^{-3}$, $L = 4$ mm, $t = 3500$ s apart from the varied parameter.

transmission in the communication field, this parameter may be negligible for lidar. It is concluded from Fig. 7(c) that the exposure time t has little effects on out-of-band rejection of FBG and the maximum reflectivity, and therefore that there is a long range of exposure time to tune the second resonant wavelength in fabricating the second-order FBG process while the second-order resonance tends to saturation. Figure 7(d) shows that the out-of-band rejection of FBG1x with $J=6$ is theoretically more than 43 dB at the laser wavelength 532 nm, which may provide a good help for rejection of more than 35 dB in practice. The out-of-band rejection of FBG2x with $J=14$ is more than FBG1x. It is also noted in Fig. 7 that while one simulative parameter is changed, the other parameters are constants, that is, $\Delta n_s = 0.8 \times 10^{-3}$, $L = 4$ mm, $t = 3500$ s, which are the recommended fabricating parameters under the specified inscribing condition in the Theoretical Analysis section for this all-fiber spectroscope.

CONCLUSIONS

An all-fiber spectroscopic filter with second-order FBG for RRL is discussed in detail. The more accurate mathematical model is created based on coupled-mode theory by evaluating the inference fringe visibility of inscribing FBG. The relationship between first-order and second-order resonant wavelength is analyzed through considering the dependence of the effective index and the core power confinement factor of the guide mode on wavelength. The better agreement of its simulative results with the experimental data reported by reference [13] verifies its correctness and improvement. A flexible configuration of the all-fiber spectroscopic filter with second-order FBG is devised for RRL. The simulative results show that the thumb principle of fabricating second-order FBG to provide at least 70 dB suppression of elastic scattering is to increase the gratings length more other than any other means, and that their saturation index variations need to be implemented as a tradeoff between the out-of-band rejection and maximum reflectivity.

FUNDING

This research was sponsored by the National Natural Science Foundation of China (NSFC) (no.

61275185, no. 41027004) and the Scientific Research Program funded by Shaanxi Provincial Education Department (no. 2010JK710).

REFERENCES

- Whiteman, D. N. Examination of the traditional Raman lidar technique. I. evaluating the temperature-dependent lidar equations. *Appl. Opt.* **2003**, *42*(15), 2571–2592.
- Balin, I.; Serikov, I.; Bobrovnikov, S.; Simeonov, V.; Calpini, B.; Arshinov, Y.; van den Bergh, H. Simultaneous measurement of atmospheric temperature, humidity, and aerosol extinction and backscatter coefficients by a combined vibrational-pure-rotational Raman lidar. *Appl. Phys. B* **2004**, *79*(6), 775–782.
- Behrendt, A.; Nakamura, T.; Tsuda, T. Combined temperature lidar for measurements in the troposphere, stratosphere, and mesosphere. *Appl. Opt.* **2004**, *43*(14), 2930–2939.
- Zeyn, J.; Lahmann, W.; Weitkamp, C. Remote daytime measurements of tropospheric temperature profiles with a rotational Raman lidar. *Opt. Lett.* **1996**, *21*(16), 1301–1303.
- Arshinov, Y.; Bobrovnikov, S.; Serikov, I.; Ansmann, A.; Wandinger, U.; Althausen, D.; Mattis, I.; Müller, D. Daytime operation of a pure rotational Raman lidar by use of a Fabry-Perot interferometer. *Appl. Opt.* **2005**, *44*(17), 3593–3603.
- Vann, L. B.; DeYoung, R. J.; Mihailov, S. J.; Lu, P.; Grobnc, D.; Walker, R. Narrowband fiber-optic phase-shifted Fabry-Perot Bragg grating filters for atmospheric water vapor lidar measurements. *Appl. Opt.* **2005**, *44*(34), 7371–7377.
- Liu, B.; Yi, F.; Yang, G. The application of fiber Bragg grating filter in lidar. *Proc. SPIE* **2004**, *5279*, 131–134.
- Mao, J.; Hu, L.; Hua, D.; Gao, F.; Wu, M. Pure rotational Raman lidar with fiber Bragg grating for temperature profiling of the atmospheric boundary layer. *Opt. Appl.* **2008**, *38*(4), 715–726.
- Malo, B.; Johnson D. C.; Bilodeau, F.; Albert, J.; Hill, K. O. Single-excimer-pulse writing of fiber gratings by use of a zero-order nulled phase mask: Grating spectral response and visualization of index perturbations. *Opt. Lett.* **1993**, *18*(15), 1277–1279.
- Hill, K. O.; Meltz, G. Fiber Bragg grating technology fundamentals and overview. *J. Lightwave Technol.* **1997**, *15*(8), 1263–1276.
- Hill, K. O. Photosensitivity in optical fiber waveguides: from discovery to commercialization. *IEEE J. Sel. Top. Quant.* **2000**, *6*(6), 1186–1189.
- Mihailov, S. J. Fiber Bragg grating sensors for harsh environments. *Sensors* **2012**, *12*(2), 1898–1918.
- Xie, W.; Douay, M.; Bernage, P.; Niay, P.; Bayon, J. F.; Georges, T. Second order diffraction efficiency of Bragg gratings written within germanosilicate fibres. *Opt. Commun.* **1993**, *101*(1–2), 85–91.
- Brady, G. P.; Kalli, K.; Webb, D. J.; Jackson, D. A.; Reekie, L.; Archambault, J. L. Simultaneous measurement of strain and temperature using the first- and second-order diffraction wavelength of Bragg gratings. *Proc. Inst. Electron. Eng.-Optoelectron* **1997**, *44*(3), 156–161.
- Echevarria, J.; Quintela, A.; Jauregui, C.; López-Higuera, J. M. Uniform fiber Bragg grating first- and second-order diffraction wavelength experimental characterization for strain-temperature discrimination. *IEEE Photo. Technol. Lett.* **2001**, *13*(7), 696–698.
- Li, M.; Janner, D.; Yao, J.; Pruneri, V. Arbitrary-order all-fiber temporal differentiator based on a fiber Bragg grating: Design and experimental demonstration. *Opt. Express* **2009**, *17*(22), 19798–19807.
- Mou, C.; Suo, R.; Zhou, K.; Zhang, L.; Bennion, I. 2nd order Bragg resonance generated in a 45° tilted fiber grating and its application. Available from: <http://www.opticsinfobase.org/abstract.cfm?URI=BGPP-2010-BTuA7>
- Jia, H.; Li, Y. First- and second-order diffraction characteristics of fiber Bragg gratings. *Opt. Commun.* **2000**, *178*(4–6), 339–343.
- Carballar, A.; Muriel, M. A. Growth modeling of fiber gratings: A numerical investigation. *Fiber Integrated Opt.* **2002**, *21*(6), 451–463.

20. Miller, G. A.; Askins, C. G.; Cranch, G. A.; Friebele, E. J. Early index growth in Germanosilicate fiber upon exposure to continuous-wave ultraviolet light. *J. Lightwave Technol.* **2007**, *25*(4), 1034–1044.
21. Kurtaran, S.; Kılıçkaya, M. The modelling of fiber Bragg grating. *Opt. Quant. Electron.* **2007**, *39*(8), 643–650.
22. Erdogan, T. Fiber grating spectra. *IEEE J. Lightwave Technol.* **1997**, *15*(8), 1277–1294.
23. Yang, L.; Huang, W.; Gu, X. The effect of radiation coupling in higher order fiber Bragg gratings. *PIERS Online* **2007**, *3*(4), 462–466.
24. Kim, D.; Cha, H. Pure rotations Raman lidar for atmospheric temperature measurements. *J. Korean Phys. Soc.* **2001**, *39*(5), 838–841.
25. Lindner, E.; Becker, M.; Rothhardt, M.; Bartelt, H. Generation and characterization of first order fiber Bragg gratings with Bragg wavelengths in the visible spectral range. *Opt. Commun.* **2008**, *281*(18), 4612–4615.
26. Kim, D.; Park, S.; Cha, H.; Zhou, J.; Zhang, W. New multi-quantum number rotational Raman lidar for obtaining temperature and aerosol extinction and backscattering scattering coefficients. *Appl. Phys. B-Lasers O.* **2006**, *82*(1), 1–4.